Pattern competition in the sequential bifurcation approach to turbulence in homogeneously heated inclined fluid and solid layers

T. Akinaga,[1,*] S. C. Generalis,[2,] and E. C. Aifantis[3,***]**

(Submitted by A. M. Elizarov)

[1] *Faculty of Engineering Science, Akita University, 1-1 Tegata-Gakuen Machi, 010-8502, Akita, Akita-Shi, Japan*
[2] *Mathematics Department, College of Engineering and Physical Sciences, Aston University, Birmingham B4 7ET, United Kingdom*
[3] *School of Engineering, Aristotle University, Thessaloniki 54124, Greece; Michigan Technological University., Houghton, MI 49931, USA; Friedrich-Alexander-University at Erlangen-Nurember, 90762 Fürth, Germany*

Received March 29, 2023; revised April 10, 2023; accepted April 15, 2023

Abstract—Non-linear solutions and their stability are presented for homogeneously heated channel flows with a simple geometry under the influence of a constant pressure gradient or when the vanishing of the mass flux across any lateral cross-section of the channel is imposed. The critical Grashof number is determined by linear stability analysis for various values of the Prandtl number. In our numerical study the angle of inclination of the channel is taken into account. We found that in each case studied, with the exception of a horizontal layer of fluid and when the applied constant pressure gradient is zero, the basic flow looses stability through a Hopf bifurcation. Following the linear stability analysis our numerical studies are focused on the emerging secondary flows and their stability, in order to identify possible bifurcation points for tertiary flows. We conclude with a few comments on revisiting the present results within an internal length gradient (ILG) framework accounting for higher order velocity and temperature gradients.

2010 Mathematical Subject Classification: 76A05, 76Dxx, 70K30, 70K50

Keywords and phrases: *Incompressible flow, Bifurcation theory, strongly nonlinear solution, stability theory, turbulence, Floquet parameters, Poiseuille flow*

1. INTRODUCTION

This work is concerned with the problem of convection in channel flows generated by uniformly distributed internal heat sources. It is partly motivated by previous studies and also by the fact that it has many important environmental and industrial applications. Homogeneous heat sources may be caused, for example, by radioactivity in nuclear reactors. Homogeneous cooling at the boundaries may lead to the same mathematical problem as internal heating as long as the fluid properties are independent of temperature [1]. The problem of internal heat generation also arises in connection with convection in the Earth's mantle. Other applications include internal heating in fluids owing to the absorption of various types of radiation such as the absorption of solar radiation in planetary atmospheres. The problem can also be compared with Benard convection, where motions are driven by temperature differences across the fluid layer and not by homogeneous heating. The present study focuses on plane parallel shear flows with homogeneously distributed internal heat sources with or without the imposition of the constraint that the mass flux across any lateral section of the channel flow is conserved. It is within this framework that internally heated parallel shear

* E-mail: akinagat@gipc.akita-u.ac.jp
** E-mail: s.c.generalis@aston.ac.uk
*** E-mail: mom@mom.gen.auth.gr

flow with a Poiseuille component is also examined. Direct comparisons of our numerical studies with published laboratory work of [2] are not possible due to the various different conditions under which the experiments were performed.

2. THEORY

We consider a viscous incompressible fluid bounded between two inclined parallel plates of infinite extent maintained at constant temperature $T = T_0$, where the cartesian coordinate system is positioned in the midplane of the fluid layer of width $2h$ with $\hat{\boldsymbol{i}}$,$\hat{\boldsymbol{j}}$ denoting the unit vectors in the streamwise and spanwise (x, y) directions respectively. In the horizontal configuration the unit vector $\hat{\boldsymbol{k}}$ points to the direction opposite to gravity and coincides with the z axis of the coordinate system. For the non-dimensional description of the problem we apply the Boussinesq approximation and we use h, h^2/ν and $qh^2/(2\kappa Gr)$, as the units of length, time and temperature, respectively. Then, the following Navier–Stokes equations for the velocity vector $\boldsymbol{u}$ and the temperature variation T from the environment are obtained [1]

$$\frac{\partial \boldsymbol{u}}{\partial t} + (\boldsymbol{u}\cdot\nabla)\boldsymbol{u}, = -\nabla\Pi + \Delta\boldsymbol{u} - \frac{\boldsymbol{g}}{g}T, \tag{1}$$

$$\frac{\partial T}{\partial t} + (\boldsymbol{u}\cdot\nabla)T = \frac{1}{Pr}(\Delta T + 2Gr), \tag{2}$$

$$\nabla\cdot\boldsymbol{u} = 0, \tag{3}$$

$$\boldsymbol{u} = 0\ ,\ T = 0 \qquad \text{at} \quad z = \pm 1, \tag{4}$$

where g is the acceleration of gravity, h the half channel width, q is the volume strength of the heat source, χ is the angle of inclination of the channel with respect to the horizontal plane. $\nabla\Pi$ is the applied the pressure gradient, ν is the kinematic viscosity, κ is the thermal diffusivity, γ is the coefficient of thermal expansion and Pr is the Prandtl number ($Pr = \nu/\kappa$). The boundary conditions are reflected by Eqs. (4), where for convenience we have set $T_0 = 0$ for the fixed temperature of the boundaries, and no-slip condition at the boundaries for the velocity field. The Grashof number Gr gives the strength of the internal heat source and terms that can be written as gradients have been combined into the expression for $\nabla\Pi$. In our formulation the Rayleigh (Ra) and Grashof numbers are related via the relation $Ra = Gr \times Pr$. The basic state for the zero mass flux (ZMF) case is described by

$$(\nabla\Pi_B)\cdot\boldsymbol{i} = -\frac{4}{5}Gr\frac{\boldsymbol{g}\cdot\boldsymbol{i}}{g}, \tag{5}$$

$$\boldsymbol{u} = U_B(z)\hat{\boldsymbol{i}} = \frac{Gr}{60}\sin\chi(5z^4 - 6z^2 + 1)\hat{\boldsymbol{i}}, \tag{6}$$

$$T = T_B = (1 - z^2)Gr, \tag{7}$$

where the the subscript B denotes the basic (laminar) flow of the system. In previous work and when the Poiseuille component is considered an alternative set of the Navier–Stokes equations are derived, where the boundary conditions of Eqs. (4) are applied and $R = -(1/2)d\Pi_B(x)/dx = U_{max}h/\nu$, is the Reynolds number that measures the strength of the applied pressure gradient in the streamwise direction (U_{max} is the maximum laminar velocity at midchannel for pure Poiseuille flow)

$$\boldsymbol{u} = U_B(z)\hat{\boldsymbol{i}} = (\tfrac{Gr}{12}\sin\chi(z^4 - 6z^2 + 5) + R(1 - z^2))\hat{\boldsymbol{i}}, \tag{8}$$

$$T = T_B = Gr(1 - z^2). \tag{9}$$

The basic velocity profile (for Eq. (8) the condition $-Gr/2 \le R \le 0$, $Gr > 0$ must be satisfied) has two inflection points in $-1 \le z \le 1$[1] and so we can expect the steady basic state to be linearly unstable, although the Rayleigh instability criteria are applicable only to inviscid cases. The equations of the disturbances are presented and non-linear equilibrium states are examined for the ZMF case only. The ZMF case corresponds to the situation where the remote ends of the channel are assumed to be closed, which in turn leads to the condition of a vanishing flow rate through the layer

[1] For $R > 0$ these inflection points lie outside the channel width and for $R < -Gr/2$ there are no inflection points.

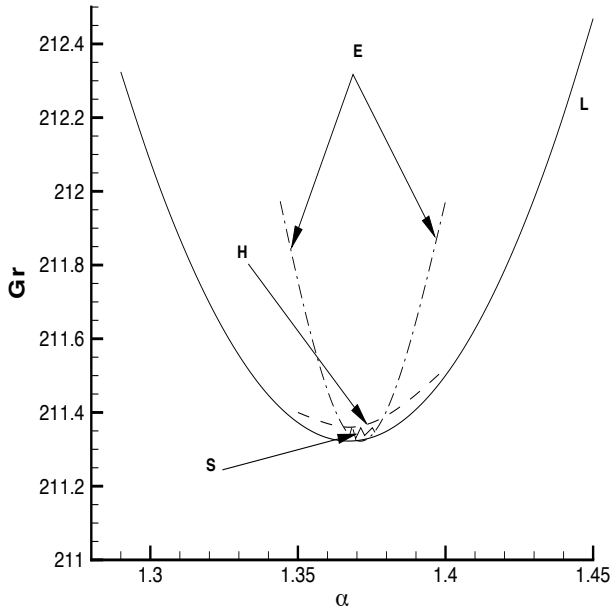

Figure 1. Instability boundaries of secondary traveling waves for $R = 0, Pr = 7, \chi = 90^0$. The stable region (shaded-S) of the secondary flow is bounded by the Eckhaus (E) and Hopf bifurcation (H) curves as indicated. For the Eckhaus boundary $d = 0.01$ while the outer boundary (L) corresponds to the stability boundary of the basic flow of Eq. (6).

cross-section. Here we present results in the case, where temperature effects are ignored ($Pr = 0$), as well as when the competing thermal instability is taken into account ($Pr = 0.1, 7$). The values of $Pr = 0, 0.1, 7$ are selected for the non-linear (stability) analysis of the states for $\chi = 0^0, 90^0$.

In order to analyse the non-linear dynamics of the two cases considered here we superimpose velocity and temperature disturbances $\hat{\boldsymbol{u}}$,$\hat{\theta}$ on the basic profiles and [3]–[5] we separate the velocity and temperature disturbances into an average part (over the x, y coordinates) $\breve{U}(z,t)$, $\breve{T}(z,t)$ and a fluctuating part $\breve{\boldsymbol{u}}$,$\breve{\theta}$ (with a vanishing average over the x, y coordinates)

$$\hat{\boldsymbol{u}} = \breve{U}(z,t)\boldsymbol{i} + \breve{\boldsymbol{u}} = \breve{U}(z,t)\boldsymbol{i} + \nabla \times \nabla \times \phi \boldsymbol{k} + \nabla \times \psi \boldsymbol{k}, \tag{10}$$

$$\hat{\theta} = \breve{T}(z,t) + \breve{\theta}, \tag{11}$$

where ϕ, ψ are the poloidal and toroidal parts of the velocity fluctuations respectively. For such a decomposition the incompressibility condition is satisfied automatically, and plays no further part in the calculations. By applying the operators $\boldsymbol{\delta} = \nabla \times (\nabla \times \boldsymbol{k}\cdot)$ and $\boldsymbol{\eta} = \nabla \times (\boldsymbol{k}\cdot)$ to Eqs. (1) we obtain the following equations for the poloidal ϕ and toroidal ψ parts of the velocity fluctuations [3]–[5]

$$\begin{aligned} \partial_t \nabla^2 \Delta_2 \phi = \nabla^4 \Delta_2 \phi - \hat{U}\partial_x \nabla^2 \Delta_2 \phi + (\partial_z^2 \hat{U})(\partial_x \Delta_2 \phi) \\ + \sin\chi \partial_{xz}^2 \theta - \cos\chi \Delta_2 \theta - \boldsymbol{k} \cdot \nabla \times \nabla \times (\breve{\boldsymbol{u}} \cdot \nabla \breve{\boldsymbol{u}}), \end{aligned} \tag{12}$$

$$\begin{aligned} \partial_t \Delta_2 \psi = \nabla^2 \Delta_2 \psi + (\partial_z \hat{U})(\partial_y \Delta_2 \phi) - \hat{U}\partial_x \Delta_2 \psi \\ + \sin\chi \partial_y \theta + \boldsymbol{k} \cdot \nabla \times (\breve{\boldsymbol{u}} \cdot \nabla \breve{\boldsymbol{u}}) \end{aligned} \tag{13}$$

while we can rewrite the temperature equation Eq. (2) in the form

$$\partial_t \theta = -\hat{U}\partial_x \theta + (\Delta_2 \phi)\partial_z (T_B + \breve{T}) + \frac{1}{Pr}\nabla^2 \theta - (\breve{\boldsymbol{u}} \cdot \nabla)\theta, \tag{14}$$

where we have dropped the $\breve{}$ from the temperature fluctuations, $\Delta_2 \equiv \partial_x^2 + \partial_y^2$ is the planform Laplacian and $\hat{U}(z,t) = U_B(z) + \breve{U}(z,t)$. Details of the numerical method followed here have been

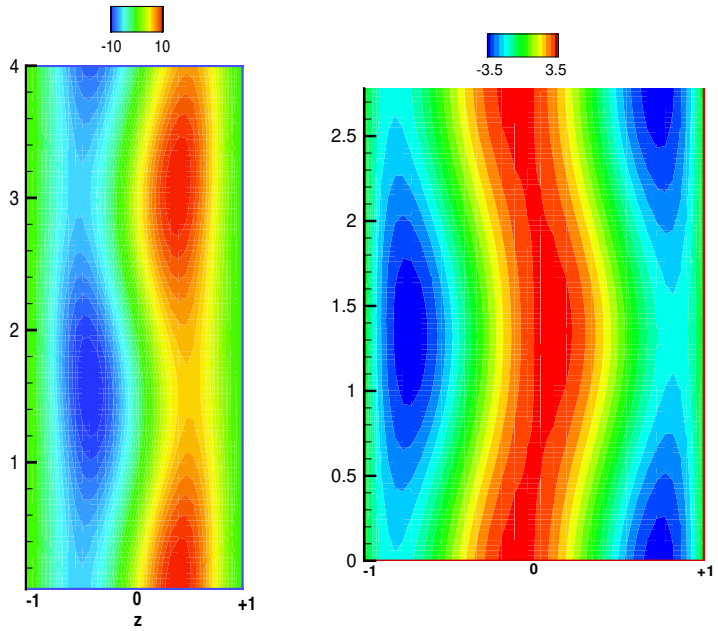

Figure 2. The stream function of the total flow (left) and the total temperature (right) of the secondary traveling wave (TW) (with $\beta = 0$). Here Gr=1850, α_c=2.07, Pr=0, $\chi = 90^0$.

reported in [3]–[5] and references therein. It is worth noting that for an orientation of the fluid layer other than horizontal the system of Eqs. (12)–(14) are solved in a moving frame of reference to account for the phase velocity of the non-linear equilibrium state.

2.1. *ZMF case:* $\chi = 90^0$, $R = 0$

In this section we calculate the non-linear equilibrium solutions that develop at the Hopf bifurcation points of the neutral curves as predicted by the linear analysis [1] due to two-dimensional disturbances (Squire's Theorem). The case $Pr = 7, R = 0$ has been considered here, for the vertical inclination of the fluid layer ($\chi = 90^0$). Here we ignore Eq. (13) and the spanwise direction (we therefore assume $\psi = \partial_y = 0$, but we retain Eqs. (13) (poloidal part). Eqs. (12) and (14) are subject to the homogeneous conditions of Eq. (3). Equations of the form [5]

$$A\boldsymbol{x} + B\boldsymbol{x}^T\boldsymbol{x} = 0, \tag{15}$$

where the unknown two-dimensional amplitudes x_i (that determine uniquely the non-linear solution) are evaluated at the collocation points $z_i = \cos((i+1)\pi/(N+2))$, $i = 0, \cdots, N$. The rank of A, B is $(L+1)(2M+1)$ and in our numerical work non-linear contributions to c, the phase velocity of the moving secondary states, are evaluated explicitly by transforming into a moving frame of reference.

In Fig. 2 we present the structure of the secondary flow for $Pr = 7$. We observe that the flow is characterized by a sequence of transverse vortices aligned along the spanwise direction. The two dimensional equilibrium solutions consist of two sets of (counter rotating) vortices of positive and negative values. This creates a 'snake'-like wavy motion that oscillates between positive and negative values of the horizontal axis z. Similar meandering effects were observed in [3]–[5] and for the case of Poiseuille flow in [6].

2.2. *$Pr = 0.1, 7$ and $R = 0$ for $\chi = 0^0$*

In this subsection we present results for the horizontal fluid layer. For this case the basic and the mean flow contributions vanish (for the ZMF case considered here $R = 0$). Moreover, because of the horizontal isotropy, there is no preferred direction for the forming patterns in the x, y-plane,

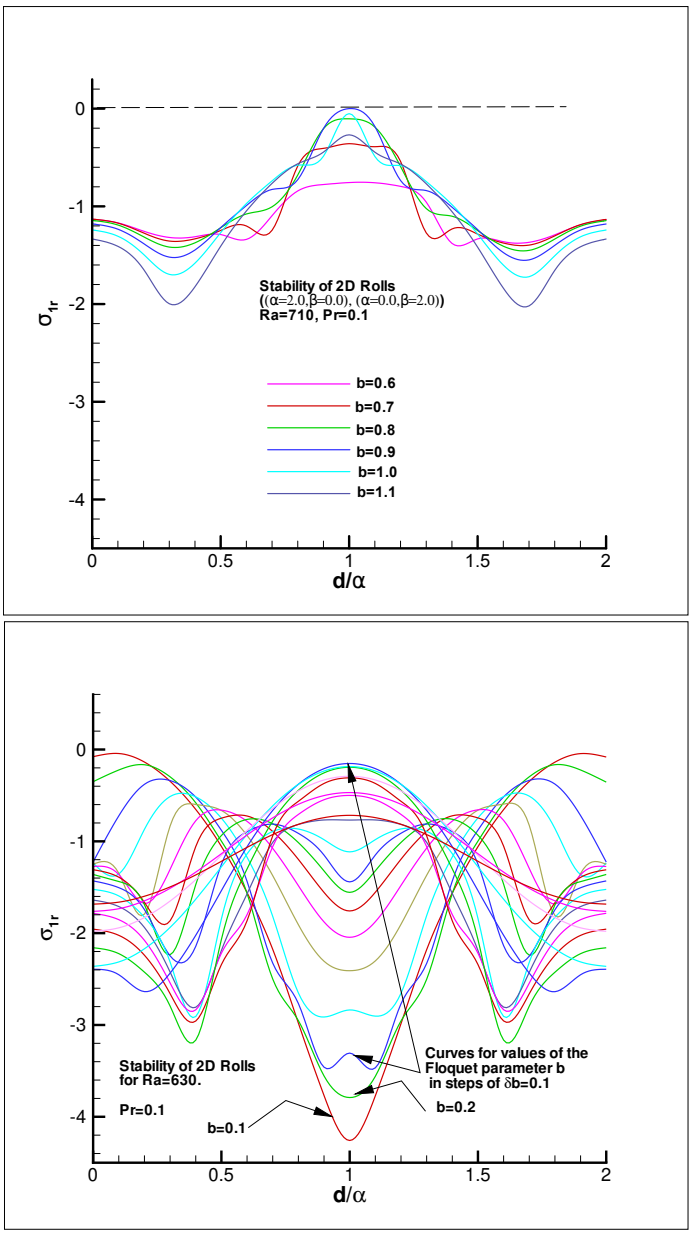

Figure 3. Plots of the most dangerous eigenvalues as a function of the Floquet parameters d, b for transverse or longitudinal rolls. Here $\alpha = 2.0, \beta = 0$, or $\alpha = 0, \beta = 2.0$, Pr=0.1, $\chi = 0°$. The value $Ra \approx 610$ is where the amplitude of the rolls approximately exceeds that of the subcritical hexagons. For $Ra > 610$ the rolls become stable, while the hexagons become unstable. The values of the parameters d, b, for which maximum growth is observed, transform the wavenumbers of the roll type cell into those of a hexagon type cell.

the eigenvalue problem is infinitely degenerate and an infinite number of convection patterns is possible in principle, as has been discussed in the analogous Benard problem by [8]. Here we just focus on the convection patterns in the form of rolls, squares and hexagons, which are the only ones which provide periodic coverage of the horizontal plane. For this case, the symmetry of the problem imposes additional constraints so that fluctuations of the following form are permitted (hereafter the superscripts $^{+}$ and $^{++}$ indicate odd or even integers respectively and for LR or TR

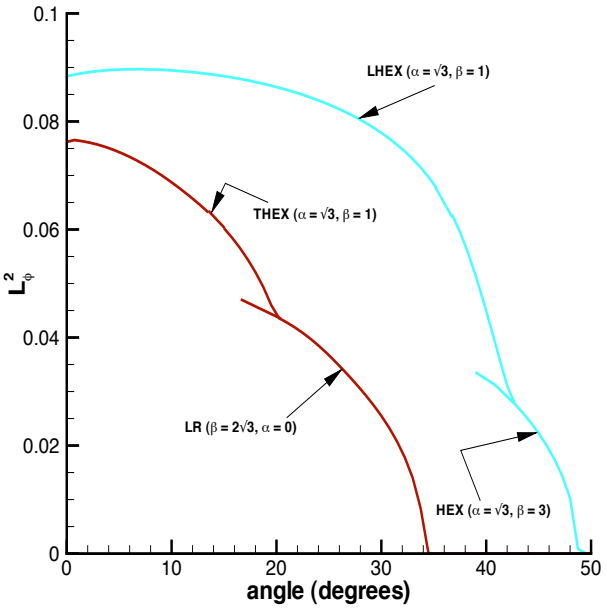

Figure 4. L_2-norm as a function of χ for the (subcritical) tertiary LHEX and THEX states. Here $Pr = 7$. As shown here the range of THEXs is much narrower than the range for LHEXs. The critical value of the anisotropy for the THEX is $\chi \approx 20^0$. The stretched pattern for the LHEX appears at $\chi \approx 33^0$. The value $Ra \times \cos\chi = 1000$ has been fixed for the calculations presented here.

type fluctuations $n = 0$)

$$\phi, \theta : \left\{ \begin{array}{lll} \cos m^{+}\alpha x & \cos n^{+}\beta y & F_{l^{+}}(z) \\ \cos m^{+}\alpha x & \cos n^{+}\beta y & F_{l^{++}}(z) \\ \cos m^{++}\alpha x & \cos n^{++}\beta y & F_{l^{+}}(z) \\ \cos m^{++}\alpha x & \cos n^{++}\beta y & F_{l^{++}}(z) \end{array} \right\}, \qquad \psi : \left\{ \begin{array}{lll} \sin m^{+}\alpha x & \sin n^{+}\beta y & F_{l^{+}}(z) \\ \sin m^{+}\alpha x & \sin n^{+}\beta y & F_{l^{++}}(z) \\ \sin m^{++}\alpha x & \sin n^{++}\beta y & F_{l^{+}}(z) \\ \sin m^{++}\alpha x & \sin n^{++}\beta y & F_{l^{++}}(z) \end{array} \right\}, \quad (16)$$

where $F_{l^{++}}(z), F_{l^{+}}(z)$ are the even and odd combinations of the expansions of ϕ, ψ, θ in terms of Chebyschev polynomials respectively [3]–[5]. Our results for the non-linear equilibrium states for $Pr = 0.1$ are given in Fig. 2 and for $Pr = 7$ are given in Fig. 1 for the vertical orientation of the fluid layer. For the horizontal orientation of the fluid layer and for $R = 0$ we found that we have a subcritical secondary state (up hexagon (HX)) that is the stable cell in contrast to the supercritical state (down HX) [7] and [8], that our numerical studies have shown that it is unstable. The competition between rolls and hexagons for different values of the Prandtl number is part of our studies. In this work we have chosen to present results for the small value for the Prandtl number $Pr = 0.1$ in order to expose possible theoretical scenarios for the stable ranges of the cells that are not evident as the Prandtl number value increases. An unexpected result is the appearance of subcritical square patterns. Our studies have shown that the square patterns become subcritical for $Pr \approx O(1)$, remaining supercritical for Pr values close to zero. The eigenvalue spectrum of the most dangerous eigenvalues as a function of the Floquet parameters (d, b) is provided for the case $Pr = 0.1, R = 0$ and $Ra = Pr \times Gr$ as indicated.

3. STABILITY OF THE SECONDARY FLOW AND DISCUSSION

The method for the numerical study of the linear stability of the secondary flow against three dimensional disturbances (in order to identify possible bifurcation points for the tertiary flow) is provided in detail in [3]–[5], [9]. In this section we have restricted ourselves to examining the stability of the flow for $Pr = 0, 0.1, 7$ and $R = 0$ for orientations of the fluid layer in $0 \leq \chi \leq 90^{\circ}$.

In Fig. 1 we discuss the stability range of transverse traveling vortices for the case of the vertical orientation of the flow channel and for $Pr = 7$ where the destabilizing effect of convection can be seen. Stable secondary states are bounded by the Eckhaus and Hopf bifurcation curves in the shaded region as indicated. For the Eckhaus curve (see Fig. 1), which bounds the area of the stable transverse travelling waves towards larger and lower wavenumbers, the spanwise Floquet parameter [3]–[5],[9] takes the value $b = 0$.

The stability of the nonlinear solutions is evaluated in terms of the sign of the real part of the most dangerous eigenvalue, σ_{1r}, when arbitrary three dimensional perturbations are applied to the nonlinear solutions, see [3]–[5], [9]. The sign of σ_{1r} dictates the stability of the bifurcating state with the state being stable if $\sigma_{1r} < 0$. Maximum growth rates for the Hopf bifurcation stability boundary were observed for $d \approx \alpha, 0.1 \leq b \leq 0.5$, when examining the stability of non-linear equilibrium states with α in the vicinity of the critical wavenumber. As in the $Pr = 0$ case our calculations have shown that for $Pr = 7$, $\sigma_{1i} \neq 0$ at the Hopf growth rate point $\sigma_{1r} = 0$. This occurrence shows that a bifurcation to a spatially periodic tertiary flow takes place that is quasi-periodic in time at the Hopf bifurcation curve boundary for $Pr = 7$.

Next we turn our attention to the horizontal configuration of the flow channel. For the case $Pr = 0$ maximum growth rates for the Hopf bifurcation stability boundary were observed for $d \approx \alpha, b = 0.2$, when examining the stability of non-linear equilibrium states with α in the vicinity of the critical wavenumber. Slight fluctuations from the condition $d \approx \alpha, b = 0.2$, when seeking the Hopf growth rate point, were observed for non-linear states with wavenumber values near the Eckhaus stability boundaries. For $Pr = 0$ $\sigma_{1i} \neq 0$ at the Hopf growth rate point $\sigma_{1r} = 0$ was also observed. This occurrence when combined with the underlying TW secondary flow shows that a bifurcation to a spatially periodic tertiary flow takes place that is quasi-periodic in time at the Hopf bifurcation curve boundary.

Next we turn our attention to the horizontal configuration of the flow channel. Three forms of convection present themselves in this case. Two correspond to hexagonal cells [up or down] one to rolls and one to a square convective pattern. Our studies for the case $Pr = 0.1$ have shown that for this case the square pattern is always unstable and that the upper branch of the subcritical hexagonal pattern is exchanging stability with the supercritical rolls in the same scenario described in [7]. When the Rayleigh number is increased the convection settles at the finite amplitude of the stable hexagon solution. In fact the subcritical hexagonal pattern becomes stable at the upper branch (from the turning point). At approximately $Ra \approx 610$ the hexagonal pattern becomes unstable. A roll component of the hexagon grows and eventually the roll replaces the hexagon. The region of stable hexagons ends and the region of stable rolls starts at the point where $\sigma_{1r} = 0$ as the Ra value increases.

In Fig. 3 we present some of the results of our stability calculations for the secondary rolls. Despite the fact that a limited number of Fourier modes and Chebyschev polynomials have been used the curves appear symmetric with respect to $d/\alpha = 0.5$. Rolls prevail for values up to $Ra \approx 710$, where they become unstable, see Fig. 3. It appears therefore that the hexagonal convection becomes more efficient than the roll form of convection for Ra values close to the critical value, the latter type becoming more efficient as the Rayleigh number is increased provided the value of the Prandtl number is small.

The reorientation of the hexagonal pattern and its transition to another hexagonal structure via the roll-route that has very recently been observed experimentally in [10], was also the subject of investigation in the present study. In [10] the reorientation has been achieved with the application of a magnetic field that is used to break the horizontal isotropy of the continuous system, the latter admitting the HX pattern as the common pattern for its instability evolution. Stretching (or reorientation) of hexagonal patterns has also been evident in the calculations presented here but for higher values of the Prandtl number. As the Pr number increases hexagonal convection becomes the predominant form of convection with the rolls being unstable. A detailed exposition of this work will be presented in the future.

In order to follow the evolution of hexagons as χ changes, in Fig. 4 we present the results of calculations for a range of values of the angle of inclination of the channel flow. In our case the anisotropy is introduced in a controlled manner by changing the value of χ. As the angle is increased two (subcritical) hexagonal patterns appear at the tertiary level in the sequence of bifurcations approach to turbulence (SBA), the L (LHEX)- and T (THEX)-type hexagons (we will

not discuss here the two supercritical hexagons that are also present for $\chi \neq 0$ as they are unstable for the range of Floquet parameter values that we examined).

The LHEXs evolve into a stretched hexagonal pattern, mainly because the wave vector for the LHEX is chracterized by the (longitudinal) roll component with the wave vector in the y-direction. Our calculations showed that the THEX solution was replaced (via a saddle-node bifurcation) by the longitudinal roll solution without any intermediary LHEX state. As was found in [9] (for a different set-up) the THEXs disappear by a saddle-node at a critical value of the angle of inclination of the channel, which determines the strength of the anisotropy.

We conclude our discussion of the results presented here by noting that as was shown in [7] the range of stable hexagonal cells vanishes as the asymmetry of material properties about the midchannel tends to zero. The selection of hexagons can therefore be attributed to the fact that homogeneous heating provides the asymmetry that removes the degeneracy within the framework of the Boussinesq approximation. Hexagons were also found theoretically and experimentally to represent a stable solution near the critical Rayleigh number in [8]. For the experiment, the property was used that homogeneous heating is equivalent to homogeneous cooling at the top and bottom boundaries. For the case where Pr exceeds a value of the order of unity and for the case of lateral heating it has been shown that both types of hexagonal patterns can be stable for $Ra = 2 \times Ra_{crit}$, see [10]–[12]. Details of the stability features of the internally heated flow in the case of other values of the inclination angle and their correlation to the value of the Pr number will be presented elsewhere.

3.1. Application of the Gradient Theory and the SBA to the Poiseuille system

Turbulent flows exhibit internal structure in the form of hairpins [13]. This suggests that it may be necessary to use continuum mechanics theories of higher order. One such possibility is to employ the internal length gradient (ILG) framework recently reviewed by one of us [14] and [15]. In the present case of incompressible Newtonian fluids, this amounts to replacing the standard expression for the stress $\boldsymbol{\tau}$ by the weakly non-local gradient expression given by the equation below

$$\boldsymbol{\tau} = -\Pi \mathbf{1} + 2\mu(1 - l_{\boldsymbol{D}}^2 \nabla^2)\boldsymbol{D}, \tag{17}$$

where $l_{\boldsymbol{D}}$ is an internal length parameter accounting for weakly non-local gradient effects and the rest of the symbols have their usual meanings ($\boldsymbol{D}$ is the symmetric part of the velocity gradient, p is the pressure and μ is the viscosity). The introduction of the Laplacian is not arbitrary, but it arises from a Taylor series expansion of a non-local integral expression for the average (macroscopic) stress which, by retaining terms up to the second order in the Taylor series expansion, is replaced by the local (microscropic) stress and its Laplacian multiplied by the internal length parameter $l_{\boldsymbol{D}}$. The determination of the new phenomenological parameter $l_{\boldsymbol{D}}$ is left to experiments and simulation, and the same holds for the new type of boundary conditions that the Laplacian term requires. As a result we have the modified, gradient enhanced Navier–Stokes (NS) equations of incompressible flow

$$\rho \frac{D\boldsymbol{u}}{Dt} = -\nabla \Pi + \mu(\Delta \boldsymbol{u} - l_D^2 \Delta^2 \boldsymbol{u}), \tag{18}$$

where, as usual, $\Delta = \nabla^2$ and $\Delta^2 = \nabla^4$ denote the Laplacian and biharmonic operators respectively. It is noted that Eq. (18) is identical to the equation used to model plane Poiseuille liquid flow at small-length scales as discussed in [15] and references quoted therein. Within the framework of ILG and for the one-dimensional flow of the Poiseuille flow system the velocity field has the form

$$u(\mathbf{x}, t) = u(z)\mathbf{e_z},$$

where $u(z)$ is the only not vanishing velocity coordinate in direction $\mathbf{e}_x$ and z is the cross-sectional coordinate of the gap. Thereby the velocity v is understood as a quantity average at a location z over a certain period of time. For plane Poisseuille flow and according to [14, 15]

$$\underline{u}(\underline{x}) = u(y)\hat{e}_x, \quad -J\frac{\partial^4 u}{\partial y^4} + \nu \frac{\partial^2 u}{\partial y^2} = \frac{\partial \Pi}{\partial x}, \quad \frac{\partial \Pi}{\partial x} = \frac{\partial \Pi}{\partial z} = 0, \quad \nabla \Pi = -\beta \hat{e}_x, \quad \beta = \text{ const} > 0.$$

Therefore,

$$-L^2v''' + u'' = -\frac{\beta}{\nu}, \quad u = c_0 + c_1 y - \frac{\beta y^2}{2\nu} + c_2 \sinh\frac{y}{L} + c_3 \cosh\frac{y}{L},$$

where $L = \sqrt{J/\nu}$ is the gradient internal length [14, 15]. The adherence conditions give

$$u(0) = u(h) = 0; \quad 2u'(0) = L^2u''(0); \quad 2u'(h) = -L^2u''(0).$$

This provides the following profile for the case of Poiseuille flow

$$v(y) = \frac{ph^2}{2f}\left\{\frac{y}{h}\left(1-\frac{y}{h}\right) - \frac{b_2}{\frac{h}{L}\sinh\frac{h}{L}}\left(\sinh\frac{h}{L} - \sinh\frac{y}{L} - \sinh\frac{h-y}{L}\right)\right\},$$

where

$$b_2 = \left(\frac{2L}{h} + \frac{2}{L}\right) / \left(1 + \frac{2}{L}\tanh\frac{h}{2L}\right).$$

We can then write $u(y) = u_{\text{classical}} + u_{\text{nonclasical}}$ or in [14, 15] terminology $u(y) = u_c + u_g; u_c = \frac{\beta h^2}{2t}\frac{y}{h}\left(1-\frac{y}{h}\right)$, which gives us the laminar profile

$$u_y = -\frac{\beta h^2}{2r}\frac{b_2 L}{h\sinh\frac{h}{L}}\left(\sinh\frac{h}{L} - \sinh\frac{y}{L} - \sinh\frac{h-y}{L}\right).$$

We will be reporting work to numerically of the numerical verification of the ILG theory adjustments to classical Navier–Stokes equations for the combined homogeneously heated Poiseuille solid-fluid problem, including non-linear effects, in the near future. This amounts into replacing the third term of the right hand side of Eq. (1) with $\Delta(T - l_T^2\Delta T)$, where l_T is a higher order gradient thermal internal length.

4. ACKNOWLEDGEMENTS

This work was funded by the RISE-Grant 824022 – ATM2BT of the European H2020-MSCA programme.

REFERENCES

1. G. Z. Gershuni and E. M. Zhukhovitskii, Convective stability of incompressible fluids. Keterpress Enterprises (1974), Jerusalem.
2. D. Wilkie and S. A. Fisher, Natural convection in a liquid containing a distributed heat source. Int. Heat Transfer Conference **Paper 119**, 995–1002 (1961). University of Colorado, Boulder.
3. M. Nagata and S. Generalis, Transition in Convective Flows Heated Internally, ASME J. of Heat Trans. **124**, 635–642 (2001).
4. S. Generalis and M. Nagata, Transition in Homegeneously Heated Inclined Plane-Parallel Shear Flows, ASME J. of Heat Trans. **125**, 795–803 (2003).
5. S. Generalis and M. Nagata, Transition in Plane-Parallel Shear Flows Heated Internally, Comptes Ren. Mech. **332**, 9–16 (2004).
6. U. Ehrestein and W. Koch, Three-dimensional wavelike equilibrium states in plane Poiseuille flow, J. of Fluid Mech. **228**, 111–148 (1991).
7. F. H. Busse, The stability of finite amplitude cellular convection and its relation to an extremum principle, J. of Fluid Mech. **30**, 625–649 (1967).
8. R. Krishnamurti, Finite amplitude convection with changing mean temperature, Parts 1 and 2. J. Fluid Mech. **33**, 445–463 (1967).
9. T.Akinaga, S.C.Generalis and F.H.Busse, Tertiary and quaternary states in the Taylor-Couette system. Chaos Solitons Fractals **109**, 107–117 (2018).
10. Y. Tasaka, Y. Kudoh, Y. Takeda, and T. Yanasigawa, Experimental investigation of natural convection induced by internal heat generation, J. Phys.: Conference Series **14**, 168–179 (2005).
11. C. Groh, R. Richter, I. Rehberg, and F. H. Busse, Reorientation of the Hexagonal pattern under broken symmetry: hexagon flip, Phys. Rev. E **76** 055301(R) (2007).

12. G. Cartland Glover, S. C. Generalis, and E. C. Aifantis, On the Convective Stability and Pattern Formation of Volumetrically Heated Flows with Asymmetric Boundaries. Lobachevskii J. Math. **43** (7), 1850–1865 (2022).
13. T. Itano and S. C. Generalis, Hairpin Vortex Solution in Planar Couette Flow: A Tapestry of Knotted Vortices. Phys. Rev. Lett. **102** 114501 (2009).
14. E. C. Aifantis, Internal Length Gradient (ILG) Material Mechanics Across Scales and Disciplines, Adv. Appl. Mech. **49**, 1–110 (2016).
15. E. C. Aifantis, Gradient Extension of Classical Material Models: From Nuclear to Condensed Matter Scales to Earth and Cosmological States, E. Ghavanloo et al. (Eds.), Size-Dependnet Continuum Mechanics Approaches, Springer Tracts in Mechanical Engineering, Springer Nature Switzerland, AG **2**, 417–452 (2021).